ACS NANO

www.acsnano.org

ARTICLE

Spin-Dependent Photovoltaic and Photogalvanic Responses of Optoelectronic Devices Based on Chiral Two-Dimensional Hybrid Organic–Inorganic Perovskites

Jingying Wang, Haipeng Lu, Xin Pan, Junwei Xu, Haoliang Liu, Xiaojie Liu, Dipak R. Khanal, Michael F. Toney, Matthew C. Beard, and Z. Valy Vardeny*

Cite This: *ACS Nano* 2021, 15, 588–595

Read Online

ACCESS | Metrics & More | Article Recommendations | Supporting Information

ABSTRACT: Two-dimensional hybrid organic–inorganic perovskites (2D-HOIPs) that form natural multiple quantum wells have attracted increased research interest due to their interesting physics and potential applications in optoelectronic devices. Recent studies have shown that spintronics applications can also be introduced to 2D-HOIPs upon integrating chiral organic ligands into the organic layers. Here we report spin-dependent photovoltaic and photogalvanic responses of optoelectronic devices based on chiral 2D-HOIPs, namely, $(R\text{-MBA})_2PbI_4$ and $(S\text{-MBA})_2PbI_4$. The out-of-plane photocurrent response in vertical photovoltaic devices exhibits ∼10% difference upon right and left circularly polarized light (CPL) excitation, which originates from selective spin transport through the chiral multilayers. In contrast, the in-plane photocurrent response generated by CPL excitation of planar photoconductive devices shows a typical response of chirality-induced circular photogalvanic effect that originates from the Rashba splitting in the electronic bands of these compounds. Our studies may lead to potential applications of chiral 2D-HOIPs in optoelectronic devices that are sensitive to the light helicity.

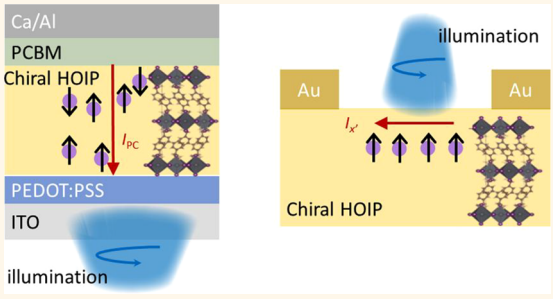

KEYWORDS: *hybrid organic–inorganic perovskites, chirality, spin transport, photovoltaic effect, circular photogalvanic effect*

Two-dimensional hybrid organic–inorganic perovskites (2D-HOIPs) are composed of alternating organic and inorganic layers, in which the electronic excitations are localized in the inorganic layers due to large potential barriers caused by the adjacent organic layers.[1,2] These materials have recently attracted increased interest due to extraordinary physics and potential optoelectronic applications coupled with solution-processed fabrication and chemical tunability that govern the active spectral range of these compounds.[3−6] Other studies have demonstrated that the 2D-HOIPs have also attractive spin-related properties, such as relatively long spin lifetime and Rashba spin splitting of the continuum bands and, therefore, may be also used for spintronic applications.[7−10] Recently, an interesting method of enhancing the spintronic properties of 2D-HOIPs has been advanced, in which chirality in the compound was introduced by chiral ligands in the organic layers that influence the electronic properties of the inorganic layers.[8,11−17]

Chirality is an important structural property of material systems. Right-handed and left-handed chiral materials have identical chemical composition and conformation, which cannot overlap by a mirror transformation; this also breaks the inversion symmetry.[17,18] It is noteworthy that chirality plays an important role in biological and pharmaceutical fields.[19,20] In addition, chirality also induces extraordinary optical and spin-related properties. For example, circularly polarized photoluminescence emission was demonstrated in chiral 2D-HOIPs, where ∼3% polarization degree was detected in the absence of magnetic field.[8,14,21,22] Also "spin filtering" has been achieved with layers of chiral material *via* the so-called chirality-induced spin selectivity (CISS), in which the transport of one electron spin species is favorable over the opposite species.[18,23−25]

Received: July 17, 2020
Accepted: November 17, 2020
Published: November 26, 2020

https://dx.doi.org/10.1021/acsnano.0c05980
ACS Nano 2021, 15, 588–595

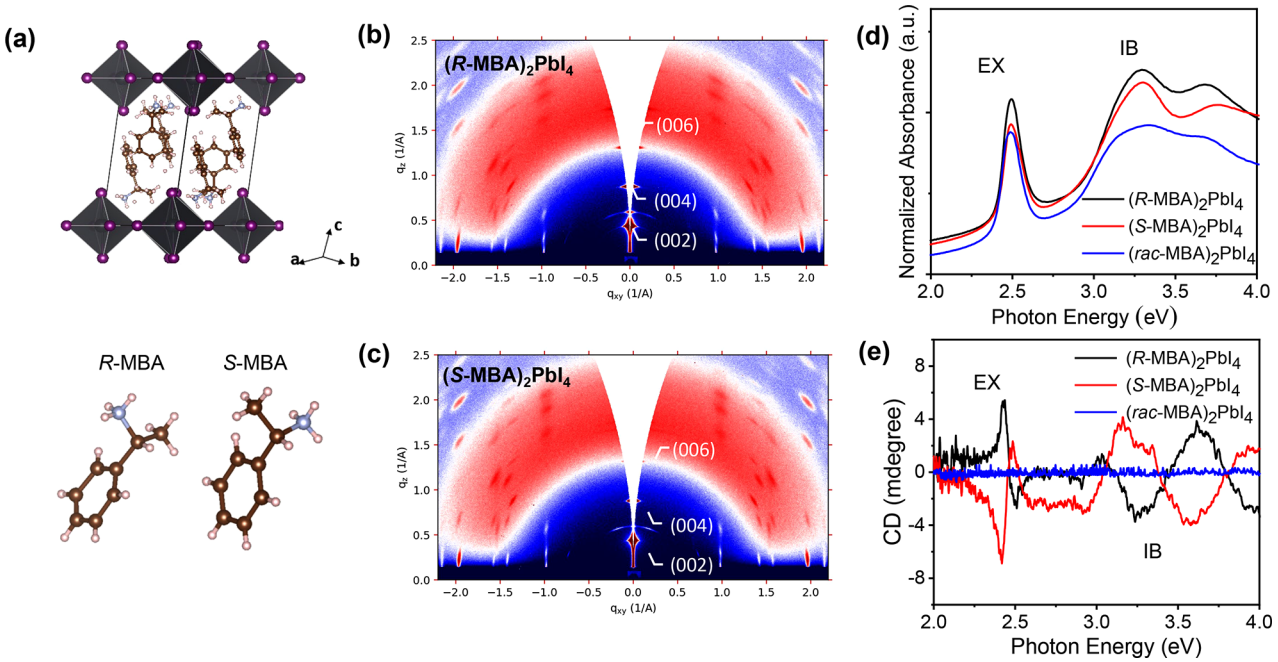

Figure 1. Structural characterizations of the chiral 2D-HOIPs. (a) Crystalline structure of the chiral 2D hybrid perovskite ((*R*/*S*-)methylbenzylammonium lead iodide, (*R*/*S*-MBA)$_2$PbI$_4$. GIWAXS of the (*R*-MBA)$_2$PbI$_4$ (b) and (*S*-MBA)$_2$PbI$_4$ (c) films. (d) Absorption spectra of (*R*/*S*/*rac*-MBA)$_2$PbI$_4$ films. (e) Circular dichroism (CD) spectra of (*R*/*S*/*rac*-MBA)$_2$PbI$_4$ films as denoted, measured at room temperature. The CD polarities of (*R*-MBA)$_2$PbI$_4$ and (*S*-MBA)$_2$PbI$_4$ are opposite to each other, whereas (*rac*-MBA)$_2$PbI$_4$ shows no CD. The absorption bands in (d) and CD bands in (e) due to exciton (EX) and interband (IB) are denoted.

Previously we reported spin-selective transport in chiral right-handed (*R*-MBA)$_2$PbI$_4$ and left-handed (*S*-MBA)$_2$PbI$_4$ methylbenzylammonium (MBA) lead iodide based spintronic devices;[11] their molecular structure is shown in Figure 1a. Due to the CISS process, we showed that the transport of one spin orientation in these 2D-HOIPs is enhanced over the other spin orientation, depending on the specific chirality of the perovskite. In the present work we study the photovoltaic and photogalvanic responses of optoelectronic devices based on these chiral 2D-HOIPs. In vertical photovoltaic devices we show that circularly polarized light (CPL) generates spin-oriented electrons and holes of which transport in the chiral 2D-HOIP device is preferentially filtered depending on the perovskite specific chirality. Consequently, the photocurrent is spin-polarized, and thus the device $I-V$ characteristic response under CPL illumination depends on the excitation light helicity and the 2D-HOIP chirality. The largest obtained difference in the device photocurrent ($\Delta I/I$) with different CPL sense was measured to be ~10% at 7 K. In contrast, photovoltaic devices based on (*rac*-MBA)$_2$PbI$_4$, which is not chiral, do not differentiate between the left- and right-handed polarization of the CPL illumination. In addition we demonstrate that the photocurrent in planar photoconductive devices based on the same chiral 2D-HOIPs is also light-helicity-sensitive, showing a typical circular photogalvanic (CPGE) response that is due to Rashba splitting in the electronic bands. Importantly, the CPGE response changes polarity for right- and left-handed chiral 2D-HOIPs, indicating that the chirality plays an important role in the inversion symmetry breaking of these compounds.[18]

RESULTS AND DISCUSSION

Materials Characterization. The chemical structure of chiral 2D-HOIPs (*R*/*S*-MBA)$_2$PbI$_4$ is illustrated in Figure 1a. The inorganic layer consists of PbI_4^{2-} octahedra, which is the same as common 2D-HOIPs. However, here the organic layer is composed of organic ligands of methylbenzylammonium, $(MBA)^+$.[26] This organic ligand comes with the left-handed and right-handed enantiomers $(R\text{-MBA})^+$ and $(S\text{-MBA})^+$, respectively, which introduce chirality into the 2D-HOIP multilayers.[27] Polycrystalline thin films of (*R*/*S*/*rac*-MBA)$_2$PbI$_4$ were formed by spin-casting of a 0.1 M solution, which is made by dissolving (*R*/*S*/*rac*-MBA)$_2$PbI$_4$ single crystals in dimethylformamide (DMF) solvent (see Methods section). Figure 1b and c show the crystalline structure characterized by grazing-incidence wide-angle X-ray scattering (GIWAXS), which presents intense Bragg spots for (*R*- and *S*-MBA)$_2$PbI$_4$ films, respectively. The observed GIWAXS results demonstrate very highly oriented crystal grains in the (*R*- or *S*-MBA)$_2$PbI$_4$ films, where the Bragg peaks may be assigned to the (h k l) peaks that are consistent with the same crystal structures observed in bulk single crystals. The extent of crystallographic texture is the same in both (*R*- and *S*-MBA)$_2$PbI$_4$ films, showing the sequence of chiral 2D-HOIP film (0 0 2l) peaks. X-ray diffraction (XRD) spectra obtained for (*R*/*S*-MBA)$_2$PbI$_4$ films are included in the Supporting Information Figure S1, as well as atomic force microscopy (AFM) images showing the films' morphology. It is seen that the crystallization and morphology of (*R*- and *S*-MBA)$_2$PbI$_4$ films are identical, and thus the observed spin-dependent optoelectronic responses described below are representative of the chiral 2D-HOIPs and not obscured by the film morphology.

The absorption spectra of (*R*/*S*/*rac*-MBA)$_2$PbI$_4$ films are shown in Figure 1d. An exciton band at ~2.5 eV is observed in all three HOIPs films, which is a common feature also in other 2D-HOIPs such as (PEA)$_2$PbI$_4$.[28,29] The films' chirality was verified using circular dichroism (CD) in transmission geometry. The CD spectra of the (*R*/*S*-MBA)$_2$PbI$_4$ films are

https://dx.doi.org/10.1021/acsnano.0c05980
ACS Nano 2021, 15, 588−595

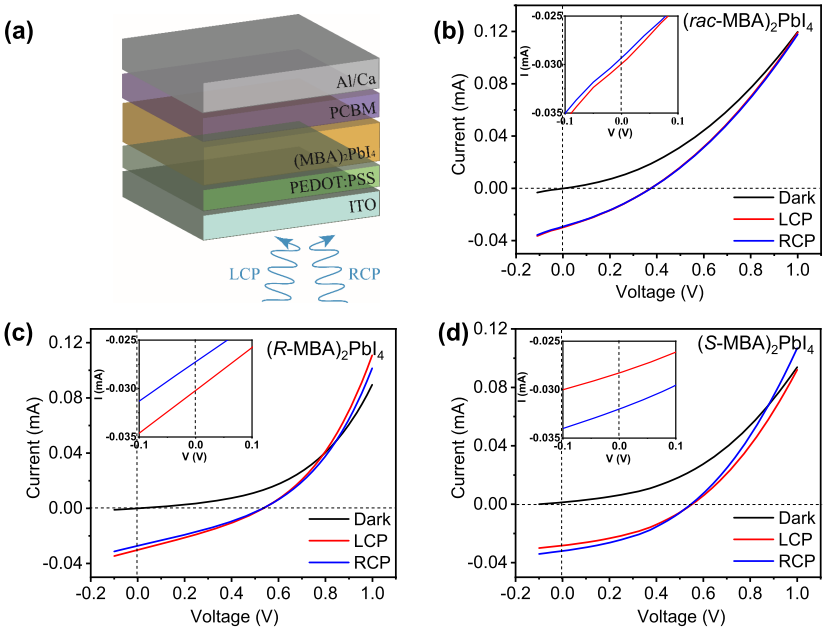

Figure 2. Structure and $I-V$ responses of the spin PV devices. (a) Schematic view of the spin photovoltaic device based on the MBA_2PbI_4 active layer. LCP and RCP light are used for the photocurrent generation. The $I-V$ response of the photovoltaic devices based on (b) (*rac*-MBA)$_2$PbI$_4$, (c) (*R*-MBA)$_2$PbI$_4$, and (d) (*S*-MBA)$_2$PbI$_4$ measured at 7 K in the dark (black), with LCP (red) light, and with RCP (blue) light using light from a 486 nm laser at an intensity of 20 mW/cm^2. The inset is a magnified view of the data around V = 0 V.

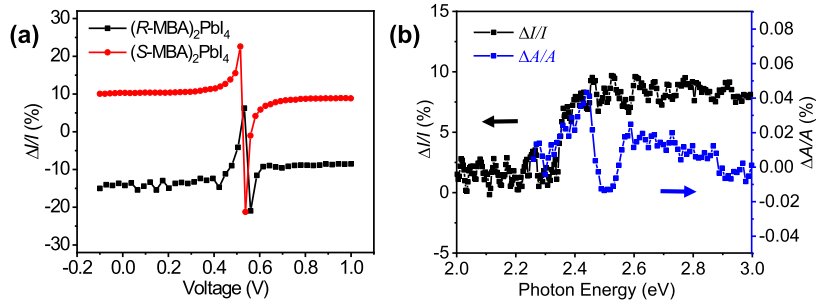

Figure 3. Voltage dependence and action spectrum of $\frac{\Delta I}{I}$. (a) Relative photocurrent difference, $\Delta I/I$, of (R/S-MBA)$_2$PbI$_4$ spin PV devices as a function of bias voltage. (b) Action spectrum of $\Delta I/I$ in an (R-MBA)$_2$PbI$_4$-based PV device compared to the relative absorption difference $\Delta A/A$ of LCP and RCP light in an (R-MBA)$_2$PbI$_4$ film measured by CD.

presented in Figure 1e. The obtained CD value is calculated from the relation[8,30,31]

$$\mathrm{CD} = \Delta A \times \left(\frac{\ln 10}{4}\right)\left(\frac{180\,000}{\pi}\right) \quad (1)$$

where ΔA is the difference in the optical density (OD) between left circularly polarized (LCP) and right circularly polarized (RCP) light. Note that (R-MBA)$_2$PbI$_4$ and (S-MBA)$_2$PbI$_4$ show CD spectra with opposite polarity. At higher photon energy (>3 eV) the CD signal is related to the optical activity of the chiral organic ligands (namely, R/S-MBA$^+$), whereas the CD signal near the exciton level (~2.5 eV) shows that there is chirality transferred from the chiral organic layers to the inorganic layers.[18] In contrast, (*rac*-MBA)$_2$PbI$_4$ does not show a sizable CD signal. We also measured Faraday rotation spectra of the chiral HOIPs that are compatible with the CD spectra near the exciton energy, as shown in the Supporting Information Figure S2.

Photovoltaic Response. The photovoltaic device structure is illustrated in Figure 2a. Indium tin oxide (ITO) was used as bottom electrode (anode), covered with a thin film of PEDOT:PSS as hole transport layer. Subsequently, (*R*/*S*/*rac*-MBA)$_2$PbI$_4$ film was spin-coated onto the structure by spin-casting. A film of phenyl-C61-butyric acid methyl ester (PCBM) as an electron transport layer is then spin-coated onto the 2D-HOIP layer. The device was capped with an Al/Ca thin film as cathode. The $I-V$ responses of (*R*/*S*/*rac*-MBA)$_2$PbI$_4$-based photovoltaic devices were measured using circularly polarized 486 nm laser light illumination with an intensity of 20 mW/cm^2 at 7 K for all measurements.

The obtained $I-V$ responses of the two chiral 2D-HOIP-based devices are shown in Figure 2c and d. In Figure 2c, it is seen that the photocurrent response in the (R-MBA)$_2$PbI$_4$-based device is different under excitation of LCP light and RCP light. We note that the intensity of the LCP and RCP light is the same during the measurements (Suppporting Information Table S1). The short-circuit photocurrent, I_{sc}, shows a difference $|\Delta I_{sc}| = |I_{LCP} - I_{RCP}| = 5.8\ \mu$A when excited using LCP and RCP illumination, respectively. Interestingly, ΔI decreases with increasing bias voltage and vanishes at the open-circuit voltage of the device ($V_{oc} \approx 0.55$ V). This shows that V_{oc} is predominantly determined by the

https://dx.doi.org/10.1021/acsnano.0c05980
ACS Nano 2021, 15, 588−595

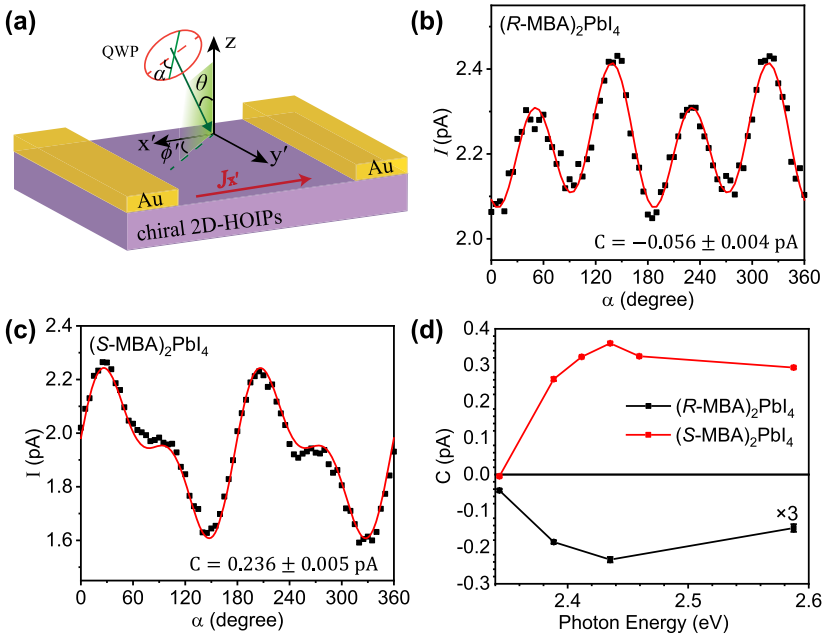

Figure 4. Circular photogalvanic effect in chiral 2D-HOIP. (a) Experimental setup for measuring the photogalvanic current using a $\lambda/4$ plate; the angles α, θ, and ϕ' are denoted. x' indicates the current flow direction. Photogalvanic current *vs* the quarter-wave plate rotational angle, α for (b) the $(R\text{-MBA})_2PbI_4$ and (c) the $(S\text{-MBA})_2PbI_4$ films, measured at 520 nm using xenon lamp excitation at room temperature. The values of the CPGE coefficient C obtained from the fitting using eq 3 are denoted. (d) Action spectra of the obtained CPGE coefficient C for the two chiral 2D-HOIPs in the spectral range of the exciton absorption band. The data for $(R\text{-MBA})_2PbI_4$ are multiplied by a factor of 3 in order to compare with the other chiral 2D-HOIP.

electrical potential difference of the two electrodes rather than the chirality of the 2D-HOIP layer or the light circular polarization. We note that the $I-V$ response has been measured multiple times on the same device and other devices to account for the variation in the measurements (Supporting Information Figures S3−S5). The $(S\text{-MBA})_2PbI_4$-based device shows a similar $I-V$ characteristic response to that of the $(R\text{-MBA})_2PbI_4$-based device except that ΔI has opposite sign (Figure 2d). As a control experiment, the same measurements were carried out on a $(rac\text{-MBA})_2PbI_4$-based device; the $I-V$ response is plotted in Figure 2b. It is seen that there is no obvious difference in the photocurrent upon LCP and RCP illumination, respectively. This indicates that the difference in the photocurrent response upon CPL illumination for $(R/S\text{-MBA})_2PbI_4$-based photovoltaic devices originates from the different chirality of the active 2D-HOIP layers.

The relative photocurrent difference $\Delta I/I$ can be calculated by

$$\Delta I/I = \frac{I_{LCP} - I_{RCP}}{(I_{LCP} + I_{RCP})/2} \quad (2)$$

where I_{LCP} and I_{RCP} are the photocurrents under LCP and RCP illumination, respectively. $\Delta I/I$ as a function of bias voltage is plotted in Figure 3a. It is seen that $|\Delta I/I|$ has a constant value of ∼10% independent of the bias voltage, with opposite sign for $(R\text{-MBA})_2PbI_4$- and $(S\text{-MBA})_2PbI_4$-based devices. Also the sharp perturbation jump around 0.55 V is due to a mathematical artifact related to the open-circuit condition, where in eq 2 the denominator I = 0 A. A plausible interpretation for the obtained significant difference in the device photocurrent response with CPL excitation is that it is related to the different light absorption caused by the CD of the chiral 2D-HOIP active layer. Since the absorption coefficients of LCP and RCP light are different in these compounds, the CPL light may photogenerate different exciton densities in the chiral 2D HOIP active layers depending on their chirality and light helicity. Consequently, upon exciton dissociation, this would lead to different photocarrier densities and, in turn, to different photocurrent for LCP and RCP excitations.[13,32,33]

To check the consequence of this interpretation, we measured the $\Delta I/I$ action spectrum, namely, $\Delta I/I$, at zero bias voltage as a function of the excitation photon energy in an $(R\text{-MBA})_2PbI_4$-based PV device. In this case a xenon lamp was used as the light source. The light was dispersed by a monochromator and then modulated by a photoelastic modulator (PEM). Since the excitation light intensity here is much weaker than the laser light intensity used before, the signal-to-noise ratio here is not as good. Nevertheless, a reliable $\Delta I/I$ action spectrum could be measured as seen in Figure 3b. For comparison, the relative absorption difference $\Delta A/A$ calculated by CD/(32 980 × absorbance) is also plotted in Figure 3b.[13,27] In contrast to the $\Delta A/A$ spectrum, the $\Delta I/I$ action spectrum has an onset at 2.4 eV and stays constant at $\Delta I/I \approx 10\%$ throughout, whereas the $\Delta A/A$ spectrum shows a clear modulation feature close to the exciton energy. The difference between $\Delta I/I$ and $\Delta A/A$ spectra demonstrates that ΔI does not originate solely from the different absorptions of the LCP and RCP light in the chiral active layer. Moreover it is clear from Figure 3b that $\Delta A/A$ is several orders of magnitude smaller than the obtained $\Delta I/I$ value of ∼10%. We thus conclude that the CD effect is not large enough to cause such a large $\Delta I/I$. In contrast, $\Delta I/I$ in the $(rac\text{-MBA})_2PbI_4$-based PV devices is not as sizable (Supporting Information Figure S8).

In our previous study, we demonstrated that chiral HOIPs can function as spin filters in spintronic devices due to the CISS effect, where the transport of electrons with one spin orientation is preferred due to the embedded chirality.[11] In the

https://dx.doi.org/10.1021/acsnano.0c05980
ACS Nano 2021, 15, 588−595

photovoltaic devices based on chiral HOIPs studied here, due to optical spin selection rules, spin-polarized carriers are generated upon CPL excitation.[9,34] Subsequently, during the transport of the spin-polarized electrons and holes through the chiral HOIP active layer, photocarriers with one spin orientation drift more easily than the other spin orientation, a process described by the CISS effect.[35] Consequently a different photocurrent response is generated when LCP and RCP light polarizations are used for a given chirality of the 2D-HOIP active layer. This phenomenon leads to spin-related optoelectronic device applications.

Circular Photogalvanic Response. We note that CISS occurs mainly for an out-of-plane photocurrent, as illustrated above; the in-plane transport in chiral HOIPs may not be as affected by CISS due to the geometry of the chiral organic ligands in the 2D-HOIPs.[25] Therefore, the in-plane photocurrent difference upon CPL illumination may not be as sizable.[3,18] On the contrary, we show here that the in-plane photocurrent is still quite sensitive to the light illumination helicity, *via* a different process, namely, the circular photogalvanic effect.[36−38] The conduction band (CB) bottom in HOIP consists of states with angular momentum $J = {}^1/_2$, whereas the states at the valence band (VB) top have spin angular momentum $S = {}^1/_2$. The optical transition selection rules for the angular momentum due to the light circular polarization require that the component of angular momentum changes by $\Delta m_J = \pm 1$. In HOIP with strong spin−orbit coupling (SOC) and breaking of the inversion symmetry, it has been established that Rashba splitting occurs in the CB and to a lesser degree also in the VB.[16,39] The circularly polarized light creates nonequilibrium spin polarization between the two Rashba branches. Since the CPL excitation with two different helicity leads to electrons having group velocity that is opposite in direction and equal in magnitude along k_x, the resulting photocurrents have opposite polarities.[7,40] At steady-state conditions and at bias voltage $V = 0$, the continuous generation of spin-polarized free carriers thus leads to photocurrent that is sensitive to the excitation light helicity; this is known as the circular photogalvanic effect, CPGE.[41] Importantly, the nonequilibrium spin-polarized photocurrent may also be generated *via* exciton absorption and subsequent dissociation if the excitons are spin polarized. This is indeed the situation in the chiral 2D-HOIP, where this mechanism falls in the category of spin-photogalvanic effect, or SPGE.[42,43]

Figure 4a illustrates the experimental setup for the CPGE measurements. A quartz quarter-wave plate (QWP) was used to modulate the light polarization of the incident light. α is the angle between the fast axis of the QWP and the incident light polarization. The light excitation intensity was modulated by a mechanical chopper at a frequency of 310 Hz. The in-plane photocurrent as a function of the angle α was measured by a phase-sensitive technique (see Methods). Importantly the photocurrent was obtained at zero bias voltage and at room temperature. We note that in addition to the CPGE (or SPGE) current associated with circularly polarized light, there is also a spin-independent photocurrent when the excitation light is linearly polarized (LP, for $\alpha = \frac{\pi}{2}n$). This is known as the linear photogalvanic effect (LPGE).[36,37] Through a 360° rotation of the QWP angle α, the incident light polarization cycles through LP, RCP, LP, and LCP, and therefore the measured photogalvanic current, $J_{x'}$, contains both CPGE and LPGE current components given by the relation[36]

$$J_{x'}(\alpha) = C \sin(2\alpha) + L \cos(4\alpha) + D \quad (3)$$

The 4α term is due to the LPGE, whereas the 2α term is generated by the CPGE; D represents a polarization-independent offset that originates from other effects such as photothermal effect, photovoltaic response, or a photo-Dember effect.[41,44−46]

Figure 4b and c show respectively the helicity-dependent in-plane photocurrent measured on planar devices fabricated on $(R\text{-MBA})_2PbI_4$ and $(S\text{-MBA})_2PbI_4$ crystal surfaces. As seen, the photocurrent changes substantially with the QWP rotation angle α. Importantly, the photocurrent response, PC, *vs* α is quite different for the two compounds with opposite chirality. Using eq 3 we fit the PC(α) response of the two chiral compounds to obtain the coefficients C, L, and D (see Supporting Information Table S2). We find a substantive contribution of CPGE in both compounds with a C/D ratio between 5% and 12%. This unambiguously shows that substantial Rashba splitting occurs in the continuum electronic bands in both chiral 2D-HOIP compounds.[16] This happens since the spin−orbit coupling is relatively strong here due to the heavy atoms in the HOIP building blocks and the lack of inversion symmetry that can be inferred from the chirality in the two compounds, a phenomenon known as chirality-driven symmetry breaking.[16] Moreover, as seen in Figure 4d the CPGE coefficient, C, has opposite sign for the two compounds with opposite chirality. This shows that the CPGE here is sensitive to the induced chirality of the 2D-HOIP, which is an exciting phenomenon. We interpret this chirality-sensitive CPGE as due to SPGE that originates from the photogenerated spin-polarized excitons. As seen in the excitation dependent on the helicity-dependent coefficient C shown in Figure 4d, the CPGE effect happens when the excitation light is on resonance with exciton absorption in the $(R/S\text{-MBA})_2PbI_4$. In this case, depending on the specific chirality of the HOIP, the photogenerated exciton density is larger with one light helicity compared to the other. Following exciton ionization the spin-polarized excitons dissociate into spin-polarized photocarriers, which, in the case of Rashba splitting, occupy a preferred half in k-space having opposite group velocity for the two circular light polarizations. This, in turn, changes the CPGE phase and thus the C coefficient polarity. This observation introduces chirality as an important factor to the field of CPGE, as well as provides a tool to investigate the existence of chirality in semiconductors.

CONCLUSIONS

In conclusion, the optoelectronic devices based on chiral perovskites integrate both exceptional optoelectronic properties of HOIPs and also spin selectivity typical of chiral materials. This provides an emerging type of photovoltaic device that is sensitive to the helicity of the circularly polarized light excitation that results in a photocurrent difference of ∼10% between LCP and RCP light illumination in devices based on chiral 2D-HOIPs. This observation demonstrates that chiral semiconductors can be used in optoelectronic devices for manipulating spin transport *via* the chirality-induced spin selectivity effect. We also showed that the chiral 2D-HOIP compounds possess a relatively large Rashba splitting in their electronic bands that is due to the large SOC and the chirality-driven inversion symmetry breaking caused by the induced chirality into the inorganic layers. This gives rise to the measured chirality-sensitive CPGE that we interpret as SPGE

https://dx.doi.org/10.1021/acsnano.0c05980
ACS Nano 2021, 15, 588−595

that originates from the selectively photogenerated spin-polarized excitons by the circularly polarized light excitation. Our studies provide an avenue to utilize chiral 2D-HOIPs in spintronic optoelectronic devices, in which spin-polarized current can be selectively photogenerated by the chirality of the chemical components and the light helicity.

METHODS

Materials. All chemicals were used as received unless otherwise indicated. (*R*)-(+)-α-Methylbenzylamine (*R*-MBA, 98%, ee 96%), (*S*)-(−)-α-methylbenzylamine (*S*-MBA, 98%, ee 98%), (±)-α-methylbenzylamine (*rac*-MBA, 99%), lead oxide (PbO, 99.999%), *N*,*N*-anhydrous-dimethylformamide (DMF), and 57% aqueous hydriodic acid (HI) solution (99.95%, distilled, stabilized by H_3PO_2) were purchased from Sigma-Aldrich.

Synthesis of $(R\text{-MBA})_2PbI_4$, $(S\text{-MBA})_2PbI_4$, and $(rac\text{-MBA})_2PbI_4$ Single Crystals. A 200 mg amount of PbO (0.897 mmol), 200 μL (1.57 mmol) of *R*-, *S*-, or *rac*-MBA, and 6 mL of HI solution were loaded into a glass vial. Then the as-formed yellow precipitates were dissolved in an oil bath at 90 °C. The solution was slowly cooled to room temperature with a cooling rate of 1 °C/h, which leads to orange needles. These crystals were vacuum filtrated and rinsed with diethyl ether. The final product was dried in a vacuum overnight.

Preparation of $(R\text{-MBA})_2PbI_4$, $(S\text{-MBA})_2PbI_4$, and $(rac\text{-MBA})_2PbI_4$ Thin Films. The substrates are cleaned by acetone and isopropanol in a sonicator for 10 min each, followed by an UV-ozone treatment for 15 min. The precursor solutions are prepared by dissolving the corresponding perovskite crystals in DMF with a concentration of 0.1 M. Thin films are then prepared by spin coating the precursor solution onto substrates with a rate of 4000 rpm for 30 s. The film is then followed by annealing at 100 °C for 10 min. Thin films on glass substrates are used for XRD and AFM measurements. Thin films on quartz substrates are used for optical (linear absorption and CD) measurements.

GIWAXS Measurements. The GIWAXS experiments were carried out in Stanford Synchrotron Radiation Lightsource (SSRL) beamline 11-3. The X-ray beam has a beam energy of 12.7 keV. The samples were deposited in NREL, shipped to SSRL, and stored in a glovebox. Before the experiments, the films were quickly brought to the beamline (within 5 min) and loaded in the N_2-filled chamber in the hatch. The position of the sample was calibrated, and the incident angle was set to 1.12 deg. A 60 s exposure was used for each 2D diffraction image. All GIWAXS results were analyzed using the pygix package in Python.

CD Measurements. CD spectra of the perovskite films were carried out by a Jasco J-715 spectropolarimeter with the thin film placed in the beam path. The spectra were smoothed using an internal algorithm in the Jasco software package J-715 for Windows. The CD spectra were monitored from 200 to 600 nm with 0.2 nm resolution, and the data are presented as the raw CD signal.

PV Device Fabrication. The ITO bottom electrode on a glass substrate was patterned by wet etch photolithography. The ITO electrode was cleaned by sonication in acetone and isopropanol for 15 min. Subsequently the bottom electrode was treated by oxygen plasma for 10 min. A thin hole transport layer, poly(3,4-ethylenedioxythiophene) polystyrenesulfonate (PEDOT:PSS, Clevios P VP AI 4083), was annealed in air for 20 min at 150 °C. The chiral perovskite film was spin-coated on the pretreated ITO electrode inside a N_2-filled glovebox (O_2/H_2O < 1 ppm). The sample was then annealed at 100 °C for 10 min. After cooling to ambient temperature, a 20 mg/mL solution of PCBM dissolved in anhydrous chlorobenzene (Sigma-Aldrich) was spin-coated at 800 rpm. The device was capped with a Ca (20 nm) and Al (100 nm) electrode that was thermally evaporated through a shadow mask with a cross configuration to the ITO electrode. The device area was 1 × 2 mm.

PV Device Measurements. Following the fabrication process the spin PV device was transferred to a closed-cycle cryostat for photovoltaic measurements. All measurements were done at 7 K, using 486 nm laser light at an intensity of 20 mW/cm^2. A quarter-wave plate followed by a polarizer was used to filter circularly polarized light. The *I*−*V* response was measured by a four-point method using a Keithley 236 power supply and a Keithley 2000 multimeter.

CPGE Device and Measurements. For the device used for CPGE measurement, two 70 nm thick gold electrodes were deposited onto the crystals by e-beam evaporation through a shadow mask in a glovebox-integrated vacuum deposition chamber (Angstrom Engineering), which had a base pressure of 3×10^{-8} Torr ($\approx 4 \times 10^{-6}$ Pa). The gap between the electrodes was 0.5 mm. For the CPGE measurements, we used as pump excitation an incandescent light source from a xenon lamp, which was dispersed through a monochromator. Roughly 25% of the light beam was focused on the active area of the device, with an area of 0.5 mm × 0.75 mm, with an intensity of ∼8.0 mW/cm^2. Due to the low intensity of the xenon lamp, we use a full-slit width of the monochromator to ensure the needed intensity for a measurable signal. The spectral resolution was estimated to be ∼10 meV.

ASSOCIATED CONTENT

Supporting Information

The Supporting Information is available free of charge at https://pubs.acs.org/doi/10.1021/acsnano.0c05980.

1. Charaterization of $(R/S/rac\text{-MBA})_2PbI_4$ samples including AFM, XRD, CD, and Faraday rotation measurements; control experiment of *I*−*V* characteristics of photovoltaic devices based on chiral perovskites; dependence of $\Delta I/I$ signal for $(rac\text{-MBA})_2PbI_4$ photovoltaic devices; summary of *L* and *D* coefficients for $(R/S\text{-MBA})_2PbI_4$ given by fitting the CPGE response (PDF)

AUTHOR INFORMATION

Corresponding Author

Z. Valy Vardeny − *Department of Physics & Astronomy, University of Utah, Salt Lake City, Utah 84112, United States;* orcid.org/0000-0002-2298-398X; Email: val@physics.utah.edu

Authors

Jingying Wang − *Department of Physics & Astronomy, University of Utah, Salt Lake City, Utah 84112, United States*

Haipeng Lu − *Chemistry & Nanoscience Center, National Renewable Energy Laboratory, Golden, Colorado 80401, United States;* orcid.org/0000-0003-0252-3086

Xin Pan − *Department of Physics & Astronomy, University of Utah, Salt Lake City, Utah 84112, United States*

Junwei Xu − *Stanford Synchrotron Radiation Lightsource, SLAC National Accelerator Laboratory, Menlo Park, California 94025, United States*

Haoliang Liu − *Department of Physics & Astronomy, University of Utah, Salt Lake City, Utah 84112, United States*

Xiaojie Liu − *Department of Physics & Astronomy, University of Utah, Salt Lake City, Utah 84112, United States*

Dipak R. Khanal − *Department of Physics & Astronomy, University of Utah, Salt Lake City, Utah 84112, United States*

Michael F. Toney − *Stanford Synchrotron Radiation Lightsource, SLAC National Accelerator Laboratory, Menlo Park, California 94025, United States;* orcid.org/0000-0002-7513-1166

https://dx.doi.org/10.1021/acsnano.0c05980
ACS Nano 2021, 15, 588−595

Matthew C. Beard − *Chemistry & Nanoscience Center, National Renewable Energy Laboratory, Golden, Colorado 80401, United States;* orcid.org/0000-0002-2711-1355

Complete contact information is available at: https://pubs.acs.org/10.1021/acsnano.0c05980

Author Contributions

This project was planned by J.W. and Z.V.V. The materials were synthesized, prepared, and characterized by H.L. and M.B. The GIWAXS measurements were done by J.X. and M.F. The device fabrication and measurements were conducted by J.W., X.P., and H.L. The PV data were analyzed by J.W., and the CPGE results were analyzed by H.L and D.R.K. The manuscript was prepared by J.W. and Z.V.V. and discussed with all other coauthors.

Notes

The authors declare no competing financial interest.

ACKNOWLEDGMENTS

This work was supported by the Center for Hybrid Organic Inorganic Semiconductors for Energy (CHOISE), an Energy Frontier Research Center funded by the Office of Basic Energy Sciences, Office of Science, within the U.S. The CPGE measurements and fabrication facility at the UofU were supported by the Department of Energy Office of Science, grant DE-SC0014579.

REFERENCES

(1) Even, J.; Pedesseau, L.; Katan, C. Understanding Quantum Confinement of Charge Carriers in Layered 2D Hybrid Perovskites. *ChemPhysChem* **2014**, *15*, 3733−3741.

(2) Wang, Z.; Lin, Q.; Chmiel, F. P.; Sakai, N.; Herz, L. M.; Snaith, H. J. Efficient Ambient-Air-Stable Solar Cells with 2D−3D Heterostructured Butylammonium-Caesium-Formamidinium Lead Halide Perovskites. *Nat. Energy* **2017**, *2*, 17135.

(3) Blancon, J. C.; Tsai, H.; Nie, W.; Stoumpos, C. C.; Pedesseau, L.; Katan, C.; Kepenekian, M.; Soe, C.M. M.; Appavoo, K.; Sfeir, M. Y.; Tretiak, S. Extremely Efficient Internal Exciton Dissociation through Edge States in Layered 2D Perovskites. *Science* **2017**, *355*, 1288−1292.

(4) Tsai, H.; Nie, W.; Blancon, J. C.; Stoumpos, C. C.; Asadpour, R.; Harutyunyan, B.; Neukirch, A. J.; Verduzco, R.; Crochet, J. J.; Tretiak, S.; Pedesseau, L.; et al. High-Efficiency Two-Dimensional Ruddlesden−Popper Perovskite Solar Cells. *Nature* **2016**, *536*, 312−316.

(5) Dou, L.; Wong, A. B.; Yu, Y.; Lai, M.; Kornienko, N.; Eaton, S. W.; Fu, A.; Bischak, C. G.; Ma, J.; Ding, T.; Ginsberg, N. S.; et al. Atomically Thin Two-Dimensional Organic-Inorganic Hybrid Perovskites. *Science* **2015**, *349*, 1518−1521.

(6) Zhang, F.; Lu, H.; Tong, J.; Berry, J. J.; Beard, M. C.; Zhu, K. Advances in Two-Dimensional Organic−Inorganic Hybrid Perovskites. *Energy Environ. Sci.* **2020**, *13*, 1154−1186.

(7) Zhai, Y.; Baniya, S.; Zhang, C.; Li, J.; Haney, P.; Sheng, C. X.; Ehrenfreund, E.; Vardeny, Z. V. Giant Rashba Splitting in 2D Organic-Inorganic Halide Perovskites Measured by Transient Spectroscopies. *Sci. Adv.* **2017**, *3*, No. e1700704.

(8) Long, G.; Jiang, C.; Sabatini, R.; Yang, Z.; Wei, M.; Quan, L. N.; Liang, Q.; Rasmita, A.; Askerka, M.; Walters, G.; Gong, X.; et al. Spin Control in Reduced-Dimensional Chiral Perovskites. *Nat. Photonics* **2018**, *12*, 528−533.

(9) Giovanni, D.; Chong, W. K.; Dewi, H. A.; Thirumal, K.; Neogi, I.; Ramesh, R.; Mhaisalkar, S.; Mathews, N.; Sum, T. C. Tunable Room-Temperature Spin-Selective Optical Stark Effect in Solution-Processed Layered Halide Perovskites. *Sci. Adv.* **2016**, *2*, No. e1600477.

(10) Chen, X.; Lu, H.; Li, Z.; Zhai, Y.; Ndione, P. F.; Berry, J. J.; Zhu, K.; Yang, Y.; Beard, M. C. Impact of Layer Thickness on the Charge Carrier and Spin Coherence Lifetime in Two-Dimensional Layered Perovskite Single Crystals. *ACS Energy Lett.* **2018**, *3*, 2273−2279.

(11) Lu, H.; Wang, J.; Xiao, C.; Pan, X.; Chen, X.; Brunecky, R.; Berry, J. J.; Zhu, K.; Beard, M. C.; Vardeny, Z. V. Spin-Dependent Charge Transport through 2D Chiral Hybrid Lead-Iodide Perovskites. *Sci. Adv.* **2019**, *5*, No. eaay0571.

(12) Long, G.; Sabatini, R.; Saidaminov, M. I.; Lakhwani, G.; Rasmita, A.; Liu, X.; Sargent, E. H.; Gao, W. Chiral-Perovskite Optoelectronics. *Nat. Rev. Mater.* **2020**, *5*, 1−17.

(13) Chen, C.; Gao, L.; Gao, W.; Ge, C.; Du, X.; Li, Z.; Yang, Y.; Niu, G.; Tang, J. Circularly Polarized Light Detection Using Chiral Hybrid Perovskite. *Nat. Commun.* **2019**, *10*, 1−7.

(14) Ma, J.; Fang, C.; Chen, C.; Jin, L.; Wang, J.; Wang, S.; Tang, J.; Li, D. Chiral 2D Perovskites with a High Degree of Circularly Polarized Photoluminescence. *ACS Nano* **2019**, *13*, 3659−3665.

(15) Wang, L.; Xue, Y.; Cui, M.; Huang, Y.; Xu, H.; Qin, C.; Yang, J.; Dai, H.; Yuan, M. A Chiral Reduced-Dimension Perovskite for an Efficient Flexible Circularly Polarized Light Photodetector. *Angew. Chem.* **2020**, *132*, 6504−6512.

(16) Jana, M. K.; Song, R.; Liu, H.; Khanal, D. R.; Janke, S. M.; Zhao, R.; Liu, C.; Vardeny, Z. V.; Blum, V.; Mitzi, D. B. Organic-to-Inorganic Structural Chirality Transfer in a 2D Hybrid Perovskite and Impact on Rashba-Dresselhaus Spin-Orbit Coupling. *Nat. Commun.* **2020**, *11*, 1−10.

(17) Lu, H.; Xiao, C.; Song, R.; Li, T.; Maughan, A. E.; Levin, A.; Brunecky, R.; Berry, J. J.; Mitzi, D. B.; Blum, V.; Beard, M. C. Distorted Chiral Two-Dimensional Tin Iodide Perovskites for Spin Polarized Charge Highly Transport. *J. Am. Chem. Soc.* **2020**, *142*, 13030−13040.

(18) Naaman, R.; Waldeck, D. H. Chiral-Induced Spin Selectivity Effect. *J. Phys. Chem. Lett.* **2012**, *3*, 2178−2187.

(19) Cahn, R. S.; Ingold, C.; Prelog, V. Specification of Molecular Chirality. *Angew. Chem., Int. Ed. Engl.* **1966**, *5*, 385−415.

(20) Kasprzyk-Hordern, B. Pharmacologically Active Compounds in the Environment and Their Chirality. *Chem. Soc. Rev.* **2010**, *39*, 4466−4503.

(21) Huang, P. J.; Taniguchi, K.; Miyasaka, H. Bulk Photovoltaic Effect in a Pair of Chiral−Polar Layered Perovskite-Type Lead Iodides Altered by Chirality of Organic Cations. *J. Am. Chem. Soc.* **2019**, *141*, 14520−14523.

(22) Dong, Y.; Zhang, Y.; Li, X.; Feng, Y.; Zhang, H.; Xu, J. Chiral Perovskites: Promising Materials toward Next-Generation Optoelectronics. *Small* **2019**, *15*, 1902237.

(23) Bloom, B. P.; Kiran, V.; Varade, V.; Naaman, R.; Waldeck, D. H. Spin Selective Charge Transport through Cysteine Capped Cdse Quantum Dots. *Nano Lett.* **2016**, *16*, 4583−4589.

(24) Xie, Z.; Markus, T. Z.; Cohen, S. R.; Vager, Z.; Gutierrez, R.; Naaman, R. Spin Specific Electron Conduction through DNA Oligomers. *Nano Lett.* **2011**, *11*, 4652−4655.

(25) Mondal, P. C.; Fontanesi, C.; Waldeck, D. H.; Naaman, R. Spin-Dependent Transport through Chiral Molecules Studied by Spin-Dependent Electrochemistry. *Acc. Chem. Res.* **2016**, *49*, 2560−2568.

(26) Billing, D. G.; Lemmerer, A. Synthesis and Crystal Structures of Inorganic−Organic Hybrids Incorporating an Aromatic Amine with a Chiral Functional Group. *CrystEngComm* **2006**, *8*, 686−695.

(27) Ahn, J.; Lee, E.; Tan, J.; Yang, W.; Kim, B.; Moon, J. A New Class of Chiral Semiconductors: Chiral-Organic-Molecule-Incorporating Organic−Inorganic Hybrid Perovskites. *Mater. Horiz.* **2017**, *4*, 851−856.

(28) Cao, D. H.; Stoumpos, C. C.; Farha, O. K.; Hupp, J. T.; Kanatzidis, M. G. 2D Homologous Perovskites as Light-Absorbing Materials for Solar Cell Applications. *J. Am. Chem. Soc.* **2015**, *137*, 7843−7850.

(29) Katan, C.; Mercier, N.; Even, J. Quantum and Dielectric Confinement Effects in Lower-Dimensional Hybrid Perovskite Semiconductors. *Chem. Rev.* **2019**, *119*, 3140−3192.
(30) Riehl, J. P.; Richardson, F. S. Circularly Polarized Luminescence Spectroscopy. *Chem. Rev.* **1986**, *1*, 1−16.
(31) Lightner, D. A.; Gurst, J. E. *Organic Conformational Analysis and Stereochemistry from Circular Dichroism Spectroscopy*; John Wiley & Sons: New York, 2000; Vol. *23*, pp 47−51.
(32) Yang, Y.; Da Costa, R. C.; Fuchter, M. J.; Campbell, A. J. Circularly Polarized Light Detection by a Chiral Organic Semiconductor Transistor. *Nat. Photonics* **2013**, *7*, 634−638.
(33) Li, W.; Coppens, Z. J.; Besteiro, L. V.; Wang, W.; Govorov, A. O.; Valentine, J. Circularly Polarized Light Detection with Hot Electrons in Chiral Plasmonic Metamaterials. *Nat. Commun.* **2015**, *6*, 1−7.
(34) Odenthal, P.; Talmadge, W.; Gundlach, N.; Wang, R.; Zhang, C.; Sun, D.; Yu, Z. G.; Vardeny, Z. V.; Li, Y. S. Spin-Polarized Exciton Quantum Beating in Hybrid Organic-Inorganic Perovskites. *Nat. Phys.* **2017**, *13*, 894−899.
(35) Naaman, R.; Paltiel, Y.; Waldeck, D. H. Chiral Molecules and the Spin Selectivity Effect. *J. Phys. Chem. Lett.* **2020**, *11*, 3660−3666.
(36) Liu, X.; Chanana, A.; Huynh, U.; Xue, F.; Haney, P.; Blair, S.; Jiang, X.; Vardeny, Z. V. Circular Photogalvanic Spectroscopy of Rashba Splitting in 2D Hybrid Organic−Inorganic Perovskite Multiple Quantum Wells. *Nat. Commun.* **2020**, *11*, 1−8.
(37) Niesner, D.; Hauck, M.; Shrestha, S.; Levchuk, I.; Matt, G. J.; Osvet, A.; Batentschuk, M.; Brabec, C.; Weber, H. B.; Fauster, T. Structural Fluctuations Cause Spin-Split States in Tetragonal $(CH_3NH_3)PbI_3$ as Evidenced by the Circular Photogalvanic Effect. *Proc. Natl. Acad. Sci. U. S. A.* **2018**, *115*, 9509−9514.
(38) Li, J.; Haney, P. M. Circular Photogalvanic Effect in Organometal Halide Perovskite $CH_3NH_3PbI_3$. *Appl. Phys. Lett.* **2016**, *109*, 193903.
(39) Kepenekian, M.; Robles, R.; Katan, C.; Sapori, D.; Pedesseau, L.; Even, J. Rashba and Dresselhaus Effects in Hybrid Organic−Inorganic Perovskites: From Basics to Devices. *ACS Nano* **2015**, *9*, 11557−11567.
(40) Yin, J.; Maity, P.; Xu, L.; El-Zohry, A. M.; Li, H.; Bakr, O. M.; Brédas, J. L.; Mohammed, O. F. Layer-Dependent Rashba Band Splitting in 2D Hybrid Perovskites. *Chem. Mater.* **2018**, *30*, 8538−8545.
(41) Ganichev, S. D.; Prettl, W. Spin Photocurrents in Quantum Wells. *J. Phys.: Condens. Matter* **2003**, *15*, R935.
(42) Golub, L. E. Spin-Splitting-Induced Photogalvanic Effect in Quantum Wells. *Phys. Rev. B: Condens. Matter Mater. Phys.* **2003**, *67*, 235320.
(43) Giglberger, S.; Golub, L. E.; Bel'kov, V. V.; Danilov, S. N.; Schuh, D.; Gerl, C.; Rohlfing, F.; Stahl, J.; Wegscheider, W.; Weiss, D.; Prettl, W. Rashba and Dresselhaus Spin Splittings in Semiconductor Quantum Wells Measured by Spin Photocurrents. *Phys. Rev. B: Condens. Matter Mater. Phys.* **2007**, *75*, 035327.
(44) McIver, J.; Hsieh, D.; Steinberg, H.; Jarillo-Herrero, P.; Gedik, N. Control over Topological Insulator Photocurrents with Light Polarization. *Nat. Nanotechnol.* **2012**, *7*, 96.
(45) Obraztsov, P. A.; Lyashenko, D.; Chizhov, P. A.; Konishi, K.; Nemoto, N.; Kuwata-Gonokami, M.; Welch, E.; Obraztsov, A. N.; Zakhidov, A. Ultrafast Zero-Bias Photocurrent and Terahertz Emission in Hybrid Perovskites. *Commun. Phys.* **2018**, *1*, 1−7.
(46) Osterhoudt, G. B.; Diebel, L. K.; Gray, M. J.; Yang, X.; Stanco, J.; Huang, X.; Shen, B.; Ni, N.; Moll, P. J.; Ran, Y.; Burch, K. S. Colossal Mid-Infrared Bulk Photovoltaic Effect in a Type-I Weyl Semimetal. *Nat. Mater.* **2019**, *18*, 471−475.

https://dx.doi.org/10.1021/acsnano.0c05980
ACS Nano 2021, 15, 588−595